

# Dual Stiffness Tensegrity Platform for Resilient Robotics

Davide Zappetti, Yi Sun, Matthieu Gevers, Stefano Mintchev, and Dario Floreano\*

Collision resilience is an important feature of robots deployed in unstructured and partially unpredictable environments. Herein, a novel dual stiffness (DS) tensegrity platform to integrate collision resilience into a robot body is proposed. The proposed DS tensegrity platform is rigid during normal robot operation, but softens upon collision to withstand the impact. The DS behavior is achieved by means of a novel DS strut that is rigid, but can buckle without breaking under high loads, thus preventing damage to the robot. Compression tests and finite element method simulations show that both the DS struts and DS tensegrities undergo substantial stiffness change with maximum load-bearing ratios up to 10.5 and 5.74, respectively, before and after buckling. These DS tensegrity structures are integrated into two types of robots, a drone and a rover, that are shown to withstand falls from 2 and 5 m, respectively. The mechanical tunability of the proposed DS tensegrity system makes it suitable for impact attenuation in a wide range of situations and robot types.

sudden collision cannot be eliminated entirely. Another approach consists of incorporating mechanical resilience into the robot body to attenuate the impact and survive the collision.

There are several strategies for adding mechanical resilience. One strategy is to use a soft body for shock absorption.<sup>[6–10]</sup> However, these soft robots can have limited load-bearing capacities.<sup>[9,11–13]</sup> Therefore, the majority of field robots, such as wheeled vehicles or drones, are still built with hard materials for higher load capacities. Another approach for mechanical resilience consists of adding an exoskeleton to a rigid robot, such as a drone.<sup>[14–19]</sup> Despite the different formats of the exoskeletons, such as deformable cages,<sup>[14–17]</sup> an origami brim,<sup>[18]</sup> or a tensegrity frame,<sup>[19]</sup> these exoskeletons result in

added mass and drag force, which inevitably reduces the flight efficiency.

Other than exoskeleton, another method for mechanical resilience is integrating dual stiffness (DS) in the mechanical structure of the robots.<sup>[20,21]</sup> A DS structure can reversibly transit between two discrete stiffness levels which has specific functionalities, as shown in the following examples. In the study by Mintchev et al.,<sup>[20]</sup> the DS mechanism is incorporated into a star-shaped frame of a quadcopter, which is locked by magnetic forces to ensure rigidity during flight. When an external load from collision exceeds a certain threshold, the magnets are disengaged, resulting in a loose frame to attenuate the impact. In the study by Mintchev et al.,<sup>[21]</sup> the DS is integrated into an origami structure with a prestretched elastic layer sandwiched in between rigid tiles. The DS is achieved and tuned by the amount of prestretching which determines the threshold that divides the rigid state for normal robot operation and the soft state for absorbing the impact from collision. The aforementioned examples show that DS is effective in collision resilience as the stiffness transitions are passively triggered upon collision and their soft states are able to attenuate the impact. Moreover, they are also weight efficient because the DS structures serve as the essential frame of the robots. However, their versatility may be limited as the tunability of the magnetic force<sup>[20]</sup> and the middle elastic layer<sup>[21]</sup> are limited.

Tensegrities are versatile structures with collision resilience functionality.<sup>[19,22–24]</sup> In the study by Zha et al.,<sup>[19]</sup> a soft icosahedron tensegrity was used as the exoskeleton of a drone. Another example is the NASA superball<sup>[22]</sup> which utilizes a tensegrity structure as the robot body and achieves collision resilience by tuning the cable tension to form a soft tensegrity. Similar examples with smaller scale can be found in other studies.<sup>[23,24]</sup>

## 1. Introduction

Robots have been utilized for the exploration of unstructured environments such as deep ocean, mine tunnels, disaster sites, and exoplanets.<sup>[1–4]</sup> However, these environments can lead to unexpected collisions that could damage the robot. To tackle this issue, protective mechanisms have been developed to those field robots. One way for protection is to utilize sensor detection and control systems to avoid obstacles.<sup>[5]</sup> However, the risk of a

D. Zappetti, Y. Sun, M. Gevers, D. Floreano  
Laboratory of Intelligent Systems  
École Polytechnique Fédérale de Lausanne  
EPFL-STI-IMT-LIS, Room MED1 1019, Station 9, Lausanne 1015,  
Switzerland  
E-mail: dario.floreano@epfl.ch

S. Mintchev  
Environmental Robotics Laboratory  
Department of Environmental Systems Science  
Eidgenössische Technische Hochschule Zürich  
LFW C 55.3, Universitätstrasse 2, Zürich 8092, Switzerland

S. Mintchev  
Swiss Federal Institute for Forest  
Snow and Landscape Research (WSL)  
Birmensdorf 8903, Switzerland

 The ORCID identification number(s) for the author(s) of this article can be found under <https://doi.org/10.1002/aisy.202200025>.

© 2022 The Authors. Advanced Intelligent Systems published by Wiley-VCH GmbH. This is an open access article under the terms of the Creative Commons Attribution License, which permits use, distribution and reproduction in any medium, provided the original work is properly cited.

DOI: 10.1002/aisy.202200025

However, those tensegrities usually have a single stiffness. When tuned into a soft structure for collision resilience, the tensegrity may lack rigidity and load-bearing capacity needed by the robot body to perform their intended tasks. Therefore, despite their versatility, single-stiffness tensegrity structures cannot be efficiently used in those rigid body-based robots for mechanical resilience. Actively controlled variable stiffness tensegrities may provide the solutions to the aforementioned issue.<sup>[25,26]</sup> In the study by Zappetti et al.,<sup>[25]</sup> low-melting-point alloy is integrated into the cables of the tensegrity and achieves a stiffness change factor up to 28 with the phase change of the alloy. In the study by Zappetti et al.,<sup>[26]</sup> a cable-driven system is installed around a tensegrity spine to change its stiffness by actively changing the constraints between the tensegrity vertebrate. However, the former requires 2.5 min for rigid-to-soft transition, which is too slow for a sudden collision, while the latter is a bulky system with additional actuators and components, which is not space and weight efficient. Therefore, a fast and passive solution is to be developed for versatile mechanical resilience using tensegrity structures.

Here, we propose a novel DS tensegrity that can be integrated within the frame of rigid robots. The proposed tensegrity is based on DS struts that are rigid under operational load conditions but can buckle at higher loads before returning to the original shape. Compression tests show a DS behavior in the struts with a maximum load-bearing (MLB) ratio of 10.5 before and after buckling. When the DS struts are used in tensegrity structures, the DS capability is passed on to the tensegrities with an overall MLB ratio of 5.74. For validation, the DS tensegrities are integrated into two types of robots, a drone and a rover, that are shown to withstand falls from 2 and 5 m, respectively. Benefiting from the versatility of tensegrity and the efficacy and efficiency of the DS concept, the proposed DS tensegrity structure could be integrated in other rigid robotic frames at strategic locations that could absorb the exceeding loads resulting from collisions with the environment.

## 2. DS Struts

The proposed method starts with designing novel tensegrity struts that provide dual stiffness by buckling. The implementable buckling types for struts under compression can be beam buckling and tubular shell buckling. In the meantime, the tensegrity structure must be recoverable after buckling, which means that the deforming part must undergo recoverable elastic deformations instead of permanent plastic ones. With these considerations, the first option is a long solid elastic strut, as shown in Figure 1A.i, but it is too soft due to a relatively low critical load. The second option is partial rigid and partial elastic strut (Figure 1A.ii). Although this design does exhibit DS behavior, the stiffness change is limited (Figure S1, Supporting Information). Therefore, for a better DS capability, a tubular structure is used for the partial elastic strut which would incur shell buckling upon compression (Figure 1A.iii). This tubular shell can remain at relatively high stiffness against compression before buckling so that it can form stiff tensegrity. Upon critical loading, it will then transit to low stiffness due to buckling. The reason for the low stiffness is that, after buckling, the circular

cross section of the tubular shell will collapse, as shown in the cross-section view of Figure 1A.iii, and start to behave like a flexural hinge.

The design of the DS struts with key dimensions is shown in Figure 1B. The tensegrities in this paper are chosen at centimeter scale. Therefore, we utilize carbon fiber (CF) rod (diameter = 1.5 mm; Young's modulus  $\approx 134$  GPa, and Poisson's ratio  $\approx 0.3$ ) as the rigid part of the struts. For the elastic part, thermoplastic polyurethane (TPU) (NinjaFlex 85A, NinjaTek; Young's Modulus  $\approx 12$  MPa; Poisson's ratio  $\approx 0.48$ ) is used as NinjaFlex 85A and has proper elasticity for adequate rigidity in the tubular shape, softness after buckling, and recoverability after load removal. The tubular TPU structures and the acrylonitrile butadiene styrene (ABS) parts for connection are prepared by 3D printing and then assembled together along with CF rod and screws into one single strut. The connections in between the components are fixed via superglue. The screws at two ends are to facilitate the connection later with the cables in the tensegrity.

Compression tests (Figure 1C) and finite element method (FEM) simulations (Figure 1D) are implemented to understand the stiffness characteristics of the struts, and the results are given in Figure 1E. The raw data of all the individual tests show that the struts can carry loads with high stiffness for about 1.37% of compression (1.1 mm), where the compression force reaches the critical load for buckling. Notably, the occurrence of the buckling is very consistent with 0.1% (0.08 mm) of standard deviation (SD) at 1.37% (1.1 mm) of compression. Before buckling, the initial stiffness of the struts against compression is calculated up to an average of  $12.24 \text{ N mm}^{-1}$  with  $0.49 \text{ N mm}^{-1}$  of SD, and the averaged critical load is 10.53 N with 0.54 N of SD. Upon the critical load, the struts start to buckle with a major crease emerging, as shown in Figure 1C.iii, which softens the struts greatly. Therefore, the compression force drops dramatically and then levels off to a small value toward the end of the tests. At 5% and 10% of compression, the force falls to an average of 3.83 and 1.94 N, respectively, while at 25%, it takes about 1 N to compress the strut, which is only 9.5% of the maximum loading and forms an MLB ratio of 10.5. On the simulation side, compared with the tube deformation in the actual experiments, the simulated deformation looks very similar. The simulation also yields very close maximum loading and initial stiffness at  $10.55 \text{ N}$  and  $14.9 \text{ N mm}^{-1}$ , respectively.

A parametric study is also conducted to understand how the tube design affects the initial stiffness and the buckling load. It is learned from the study by Timoshenko et al.<sup>[27]</sup> that changing the length, diameter, and wall thickness of the tube will all result in different buckling characteristics. First, increasing the tube length will lower the buckling force. Therefore, a longer tube will make the buckling too easy. Meanwhile, a shorter tube with a long CF rod does not allow sufficient amount of compression. Second, within the scale of the tensegrity built in this work, increasing the tube thickness/diameter will increase the buckling load and the initial stiffness due to the increased cross-section area. However, considering the tensegrity size, there is not much space for the change of tube diameter. Therefore, tube length and diameter are not included in the parametric study. Instead, we fix the inner diameter and vary the tube wall thickness. Considering the similarity between the experimental and simulated results, the parametric study is implemented in

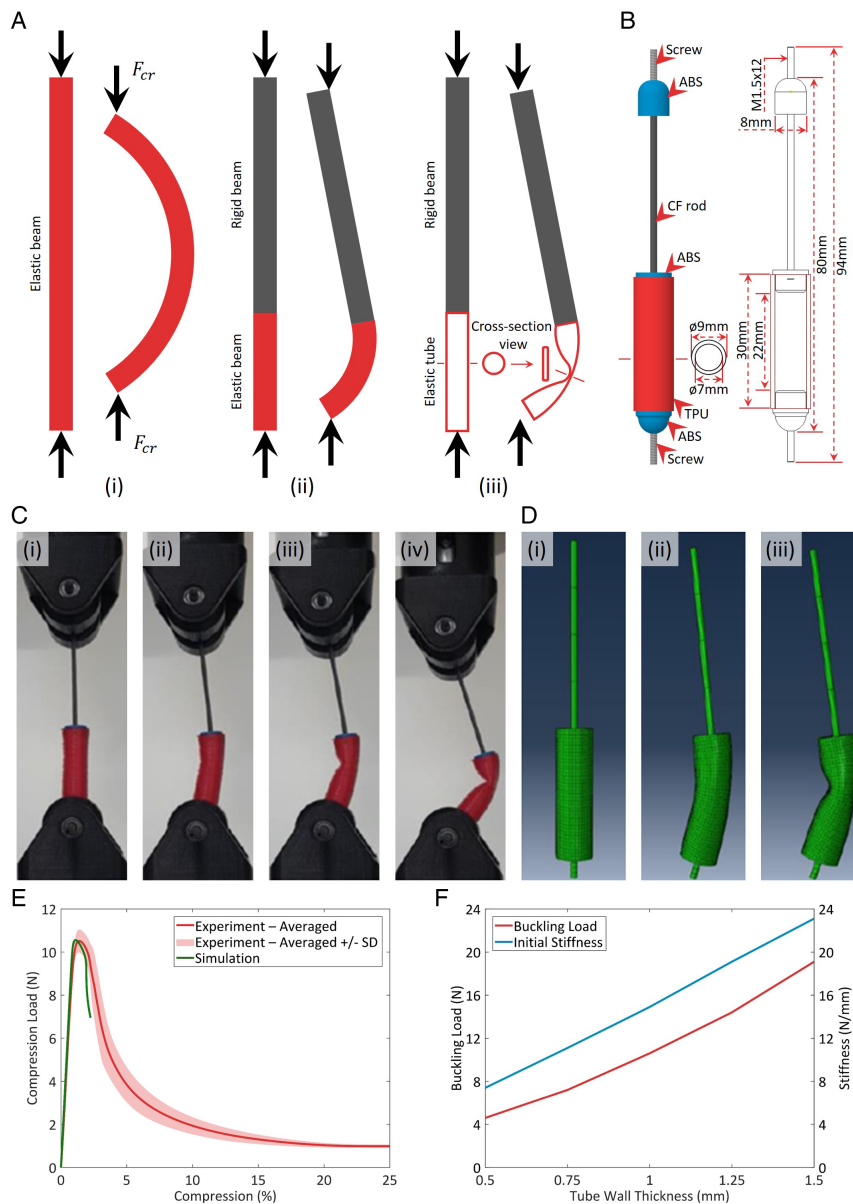


**Figure 1.** DS strut design and characterization. A) Three buckling choices for DS strut: (i) long elastic beam as the whole strut; (ii) partially rigid and partially elastic beam for the strut; (iii) partially rigid and partially elastic tube for the strut. B) Strut design with material selection and key dimensions. C) Experimental test, D) FEM simulation, and E) their results of the compression of the struts with the same materials and dimensions, as depicted in (B). F) The results of strut parametric study with fixed tube length (22 mm), inner diameter (7 mm), and varied tube wall thickness.

simulation. The results are given in Figure 1F, which shows that the initial stiffness and buckling loads are almost linearly increased with the tube wall thickness. By changing the tube wall thickness from 0.5 to 1.5 mm, the buckling force and initial stiffness increase from 4.6 to 19.1 N and from 7.4 to 23.1 N mm<sup>-1</sup>, respectively. Notably, the ranges of tested wall thicknesses are only specific to the tensegrities and robots in this study, while tensegrities can be formulated into different sizes and shapes. Therefore, this parametric study cannot cover the whole scope of strut designs. However, the same procedure can be followed for new strut designs for resilient tensegrities with DS function.

### 3. DS Tensegrity Structures

The second task is to integrate the DS struts into a tensegrity so that it will inherit the DS feature. We choose the simple triangular prism tensegrity, as shown in Figure 2A. For each tensegrity, the three struts are the DS struts with the same design and dimensions, as described in Figure 1B, while the nine cables with two holes at two ends (hole-to-hole length = 55 mm) are laser cut from Kapton sheets (Kapton 400HN, Dupont Inc.; thickness = 100 μm; Young's modulus ≈ 2500 MPa; Poisson's ratio ≈ 0.34). After manual assembly, the ends of the Kapton

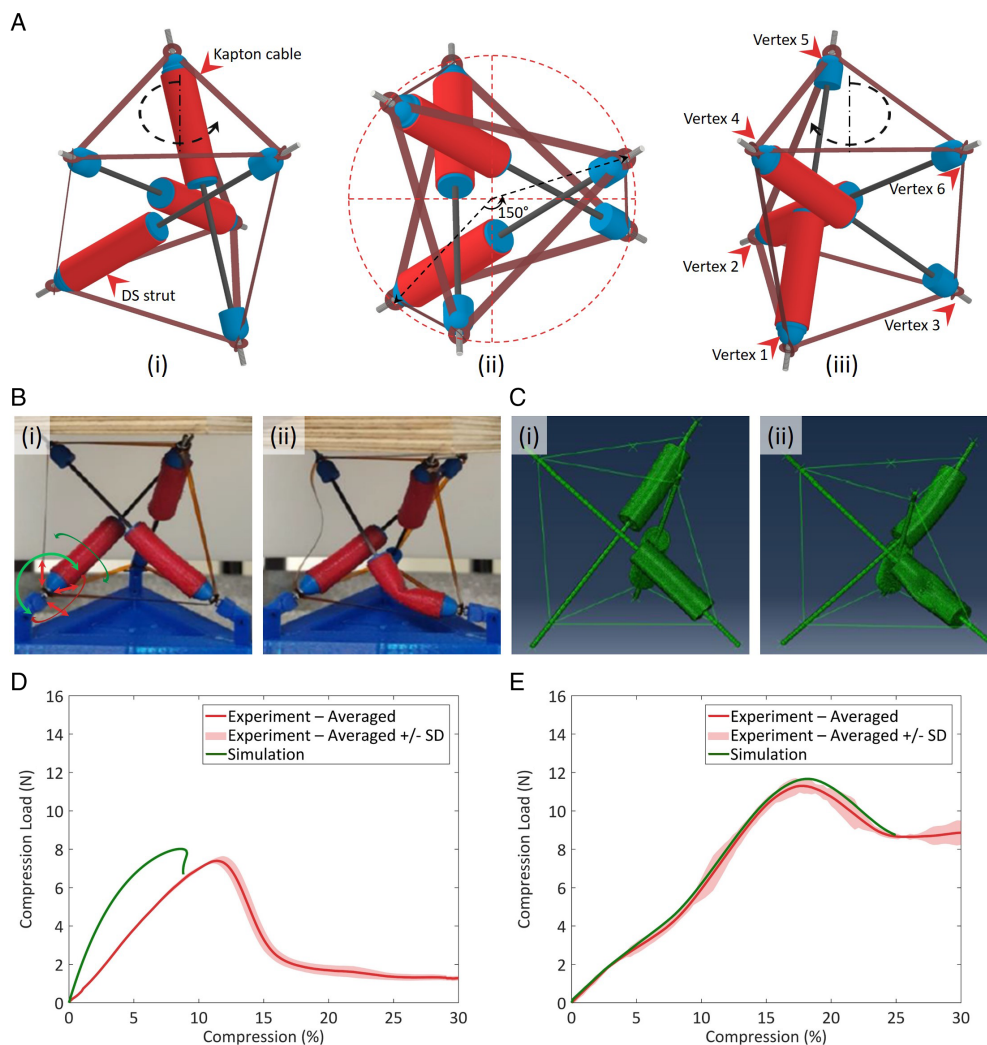


**Figure 2.** DS tensegrity design and characterization. A) The DS tensegrity, made from DS struts and Kapton cables, is designed into (i) a triangular prism with (ii)  $150^\circ$  twisting angles between the top and bottom triangles in CCW and (iii) CW directions. B) Experimental test and C) FEM simulation of the compression on the DS tensegrity. The green and red markers in B(i) represent free and constrained degrees of freedom, respectively, for the vertices on the hinge joints. D) Top and E) side compression and simulation results. For side compression, the tensegrity is compressed with vertices 3 and 6 on the top and vertices 1, 2, 4, and 5 facing the bottom.

cables and struts are fixed together with nuts tightened on the screws at the ends of the struts.

Compression tests from the top (Figure 2B) and side are implemented on the tensegrity modules along with FEM simulation (Figure 2C). According to the results as shown in Figure 2D,E, there are DS features in tensegrities, regardless of their orientations during the tests. For the top compression test, although three struts are compressed simultaneously, the average maximum buckling load is only 7.4 N, which is less than the force to press one vertical strut (Figure 1E). This is mainly because, in the tensegrity, the struts are fixed in the inclined orientations and thus the forces are divided into vertical and horizontal components. The compression tests record the sum of the vertical force components, while the horizontal components are counteracted by the tensions in the horizontal cables. Moreover, the averaged initial stiffness also becomes much

smaller ( $\approx 2.1 \text{ N mm}^{-1}$ ) with delayed buckling at around 11.5% of compression, which is also because of the strut orientation. After buckling load, the force quickly drops to 2 N at 17% as the soft state of the tensegrity. At 30% of compression, the force is only 1.29 N, which is only 17.4% of the maximum loading and forms an MLB ratio of 5.74. On the other hand, the simulation results give a higher initial stiffness ( $\approx 2.8 \text{ N mm}^{-1}$ ), though the buckling force ( $\approx 8 \text{ N}$ ) is similar to the experiments. This difference may come from the manual assembly of the tensegrity.

For the side compression, the buckling load, averaged at around 11.3 N, is higher than the top compression tests. In addition, the simulation results stay close to the experimental data. With further delayed buckling at around 17.5%, the averaged initial stiffness drops to around  $1.1 \text{ N mm}^{-1}$  only. Unlike the previous curves which are almost straight before buckling, the

curve of the side compression turns slightly steeper at around 7% of compression. This is because, at the beginning of the side compression tests, only three vertices touch the bottom, and, with further compression, the fourth vertex falls in contact with the ground and contributes to the overall stiffness. Notably, during the side compression tests, we observed jamming between the struts after buckling, which caused a higher compression force at around 8.5 N toward the end of the tests. Therefore, the dual stiffness feature is not very strong in the side compression case. However, we believe this only happens to that specific orientation as the three buckling tubes are all gathered at the bottom side along the force direction. In the other orientations, such as the top compression case, the tubes are loosely distributed along the force direction, which allows the free buckling of the tubes and low stiffness in the buckled state of the tensegrity.

#### 4. DS Tensegrity Robots with Resilience

The proposed DS tensegrity structures are integrated and validated in two types of robots, a drone and a wheeled rover, whose collision resilience is assessed in compression and crash tests.

##### 4.1. DS Tensegrity Drone

As shown in **Figure 3A**, the body of the DS tensegrity drone is composed of four DS triangular prism tensegrities developed in Section 3 (two clockwise [CW] ones and two counterclockwise [CCW] ones arranged diagonally). The tensegrities are connected to one another via 3D-printed hinge joints (ABS) to allow deformation during buckling upon collision (**Figure 3A.ii**). The four propellers (Durable Prop T2.5X3.5X3, HQProp Co., Ltd) and motors (BE1104-4000KV, DongYang Smart Technology Co., Ltd) are fixed at the four connection points where the tensegrities meet on the top surface. The AIO Brushless Flight Controller (F4 2-4S 12A, BetaFPV Co.,Ltd) and battery are placed at the center of the four-tensegrity frame (**Figure 3A.iii**). The whole frame weighs 30 g with dimensions of 130 × 150 × 70 mm, and the whole robot is 105 g.

Compression tests from the top (**Figure 3B**) and side are implemented to assess the DS characteristics of the drone, and the results are given in **Figure 3C**. It is clear from the compression results that the body frame, made of four DS tensegrities, has the DS behavior. In top compression, the load increases tortuously with two-step initial stiffness, 3.84 N mm<sup>-1</sup> from 0% to 4% and 1.54 N mm<sup>-1</sup> from 9% to the overall buckling point of 14.5%. During the top compression test, all the DS struts are compressed simultaneously, and due to some errors in the fabrication and assembly, one or two struts partially buckle before the overall buckling point according to our observation, which results in the two different initial stiffness. Although this quasi-sequential buckling of the struts reduces the overall stiffness (2 N mm<sup>-1</sup> from 0% to 14.5%), this feature can potentially enhance the buffering of the impact and the resilience of the robot. The maximum buckling load is recorded at an average of 26.04 N, which is similar to four times the buckling load of the top compression from the single tensegrity (**Figure 2D**). After buckling, the force decreases almost linearly to 10.7 N at

30% of compression. On the other hand, the side compression yields a slightly exponential increase of the force before the buckling. This is because the testing orientation of the tensegrity frame, as shown in **Figure 3A.iv**, has more space to squeeze, which also explains the delayed buckling point at 27%. The overall initial stiffness from 0% to 27% is around 0.65 N mm<sup>-1</sup> and the maximum buckling load is recorded at 22.74 N. After buckling, the force quickly drops to about 17 N at the end of the test.

Furthermore, the crash-landing experiments are performed to test the collision resistance of the drone. The ultimate height the drone can survive is up to 2 m, which corresponds to a crash speed of 6.3 m s<sup>-1</sup>, above which the connectors of the motors would break. From the sequential snapshots (**Figure 3D**) of the 2-meter-height crash test (**Video 1**), we can see that the struts stay straight at the initial contact with the ground and then buckle when the impact force goes over their critical load. In the process of the crash, the struts are not compressed at the same time; therefore, as shown in the snapshots in **Figure 3D**, they buckle at different time points and some of them may not buckle. Due to the buckling of the struts, the impact attenuation is effective according to **Figure 3D.vi**, in which the maximum rebound height is only 15 cm (potential energy ≈0.15 J) as compared with the 2-m free-fall height (potential energy ≈2 J), meaning that 92.5% of the energy is absorbed by the tensegrity due to strut buckling. In the air, the robot is fully recovered to its original shape for new flights due to the elasticity of the strut material, meaning resilience is achieved. Also, from **Figure 3D.v** which is the moment right before the rebound, we can see that the direct contact between the electronics and the solid ground is avoided, which represents the strong protection by the tensegrity frame.

##### 4.2. DS Tensegrity Rover

The tensegrity rover, as shown in **Figure 4A**, is composed of two DS tensegrity modules developed in Section 3, one CW and one CCW. They are also connected via 3D-printed hinge joints (**Figure 4A.iii**) at the three vertices of the triangular face, making a symmetric body frame that weighs 15 g with dimensions of 120 × 60 × 60 mm. The 3D-printed wheels (NinjaFlex 85A) and the motors (Pololu 5601, Pololu Corp.) are attached at the two sides, while the electronics (TinyDuino processor board, TinyCircuits Inc.) are fixed at the center. From the electronics fixation, a 3D-printed tail (NinjaFlex 85A) is extended out of the body with a battery case at the end. This tail along with the battery serves as a stabilizer to prevent the self-rotation of the body frame during the motor movement. With full assembly, the rover weighs 110 g and runs at 1.7 m s<sup>-1</sup> at full speed.

The rover also undergoes compression tests from the top and the side (**Figure 4B**), and the results are given in **Figure 4C**, from which, we can see that, because of the DS tensegrities, the rover body frame also has the DS property in both compression directions. In the top compression, the force increases almost linearly toward the buckling point at around 11% of compression. The initial stiffness calculated from 0% to 5% is about 3.55 N mm<sup>-1</sup> and the maximum buckling load is 16.81 N. After buckling, the force starts to drop and reaches a trough of 9 N at around 20% of compression, after which the force slowly increases because the struts and the electronics are

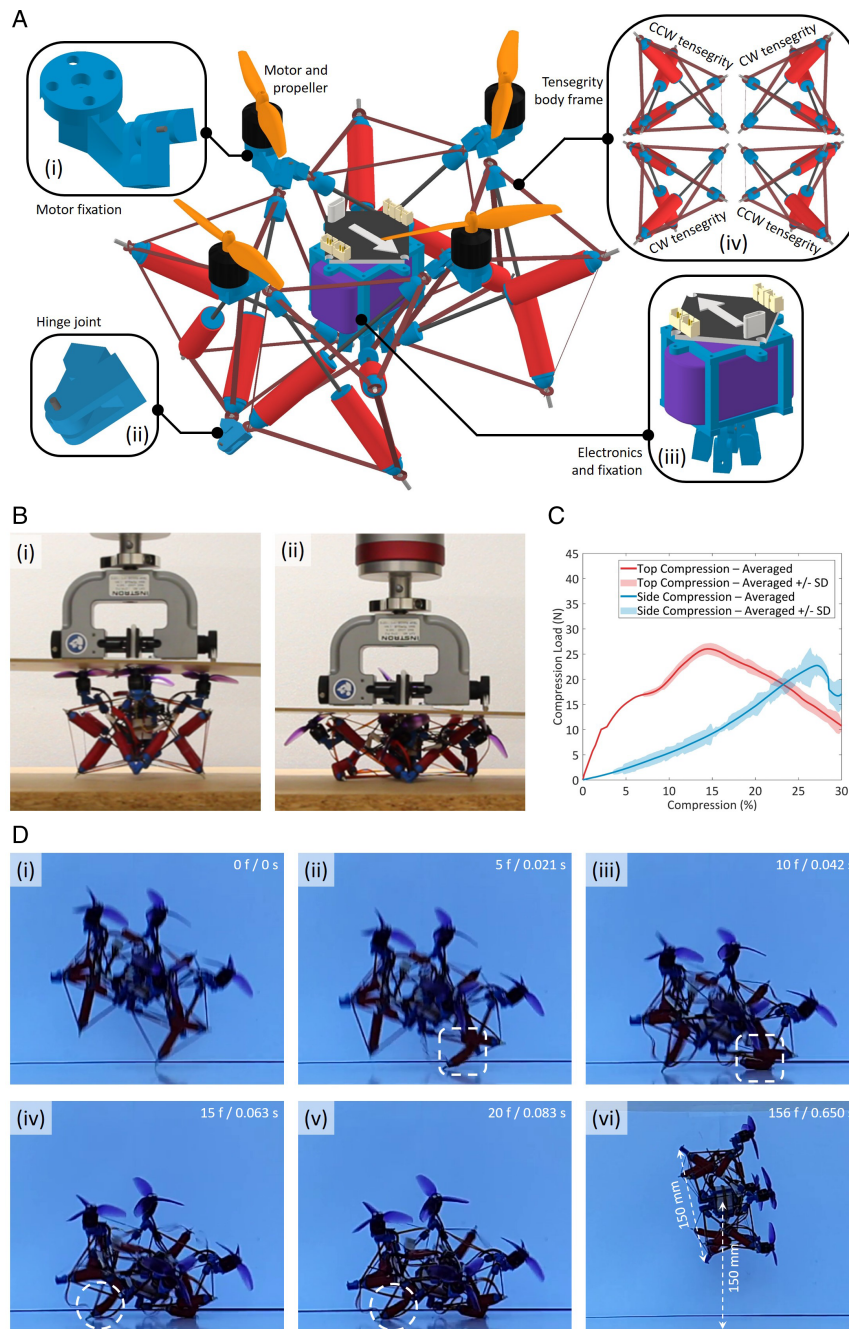


**Figure 3.** Design and tests of DS tensegrity drone. A) DS tensegrity drone design. (i) The motor fixations are extended from (ii) the hinge joints that connect the vertices of the tensegrities. (iii) Electronics fixation has four hinge joints at its bottom to connect with the four vertices of the four tensegrities at the bottom surface. (iv) Tensegrity body frame. B) Top compression test. C) Results from top and side compression. For side compression, the drone is compressed in the orientation as shown in (A.iv). D) Snapshots of crash test of the drone falling from 2-meter height (Video 1). (i) to (v) are captured from the first contact with the ground to the state right before the rebound with five-frame intervals. The first and second buckled struts during the crash are pointed out by the white dotted circle and square, respectively. (vi) shows the highest rebound of the drone.

squeezed to contact one another. For the side compression, although the tensegrities on the top and bottom are being compressed together, the results are fairly similar to the top compression of a single tensegrity in Figure 2D, as expected with a close buckling load at 9.57 N. There are also some differences caused

by the addition of the two wheels and inner electronics. The additional height from the wheels reduces the initial stiffness to around  $1 \text{ N mm}^{-1}$  and advances the buckling point to around 7.4% of compression. After buckling, the compression force falls and then, due to the contacts between different components,

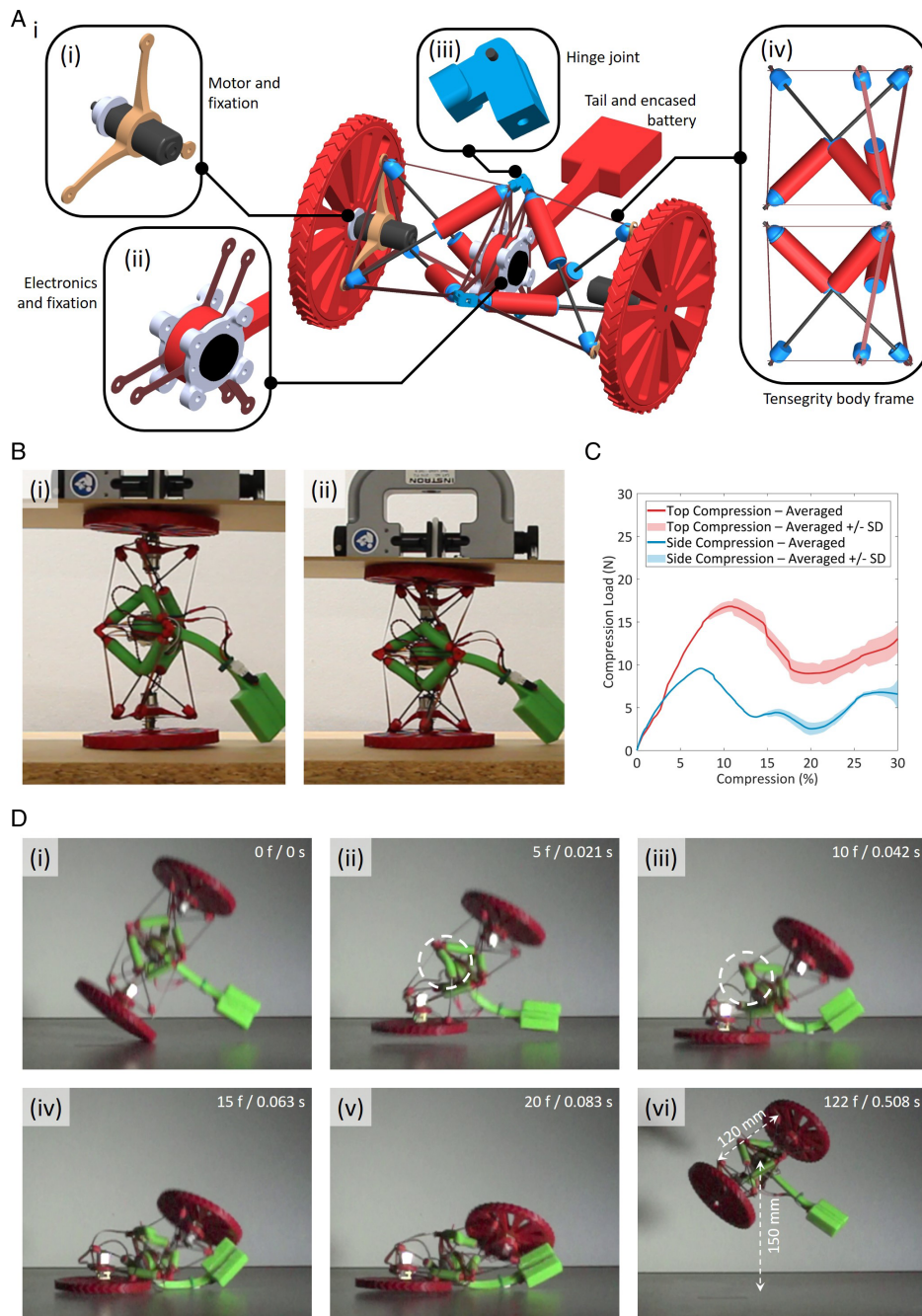


**Figure 4.** Design and tests of DS tensegrity rover. A) DS tensegrity rover design. The motor for the wheel is fixed onto the tensegrity body frame via (i) a 3D-printed three-pointed TPU part (NinjaFlex 85A), while the electronics is fixed at the center via (ii) two three-pointed Kapton sheets made from laser cutting. (iii) Hinge joints are also used to connect the two tensegrities into (iv) the robot body frame. B) Side compression test. C) Results from top compression and side compression. For top compression, the rover is compressed in the orientation, as shown in (A) without the wheels. D) Snapshots of crash test of the rover falling from 2 m height (Video 2). (i) to (v) are captured from the first contact with the ground to the state right before the rebound with five-frame intervals. The buckled strut during the crash is pointed out by the white dotted circle. (vi) The highest rebound of the rover.

forms a wavy curve with a minimum force of 2.5 N at 20% of compression and a maximum force of 6.8 N near the end of the tests.

The crash-landing experiments are also performed on the rover to test the collision resistance capability. The rover can survive a height up to 5 m (crash speed of  $9.9 \text{ m s}^{-1}$ ) which is better

than the drone case. This elevated resilience may partially result from the soft wheels which can also buffer the impact. Tests above 5 m result in the breakage of the Kapton cables. From the sequential snapshots (Figure 4D) of the 2 m-height crash test (Video 2), we can see a similar reaction of the tensegrities with initially straight struts at the first contact with the ground buckle

upon the impact force. In the case of the rover, the body is severely flattened due to the impact, as shown in Figure 4D.v, which reveals the softness of the body frame after buckling. However, such buckled softness does not mean fragility; instead, it serves as an effective buffer, demonstrating the intelligence of the body frame for protection from instant impact. Again, due to buckling of the struts, the impact attenuation is effective according to Figure 4D.vi because the rebound height, similar to the drone case, is also around 15 cm (potential energy  $\approx 0.16$  J), as compared with the 2 m free-fall height (potential energy  $\approx 2.16$  J), meaning that 92.6% of the energy is absorbed by the tensegrity due to the strut buckling. The resilience is then fully achieved with the robot restoring its original shape after the impact (Figure 4D.vi). Video 2 shows the rover falls from 5 m height and quickly moves again after crashing on the ground which validates the collision resilience of the robot.

## 5. Conclusion

In this article, we proposed a new kind of mechanical intelligence for collision resilience by means of a DS tensegrity structure with buckling struts. The design of the struts with partial rigid beam and partial tubular shell for buckling resulted in a DS behavior with an MLB ratio of 10.5 between the initial stiff state and buckled soft state. The DS struts were then installed into tensegrity structures. Due to the inclined orientation of the struts, the stiffness of the struts is divided into the stiffness of the tensegrity in different directions. Therefore, the compression tests yielded varied stiffness characteristics of the tensegrity with an MLB ratio up to 5.74. The DS tensegrities were integrated into two robots, a drone and a rover, and allowed them to withstand falls from up to 2 and 5 m, respectively.

The proposed DS tensegrity for collision resilience could find applications at different scales and fields. For example, large DS tensegrity structures could serve as scaffolds for lightweight modular bridges, infrastructures, manipulators, antennas, and buildings with the ability to survive unexpected external loads. Human-scale DS tensegrities are promising for modular robotic frames and other structures such as wings, arms, tails, and fingers that need collision resilience, while smaller-scale DS tensegrity structures could be useful for minimally invasive surgery devices where the ability to soften passively after a certain load threshold can ensure safety and protect tissues.

## 6. Experimental Section

*DS Struts Compression Test and FEM Simulation:* The DS struts were tested on Instron 5965 (Instron Inc.) with a compression rate of  $20 \text{ mm min}^{-1}$ . Three strut samples were tested with three repetitions each. During the tests, two ends of the struts were fixed onto the hinge joints (Figure 1C) to allow rotation of the two ends to emulate the scenario when the struts were in the tensegrity, which would yield referenceable stiffness data. A compression displacement of 25% of the length was applied from the top of the strut and the compression force along the vertical axis was recorded. Strut compression simulation (Figure 1D) was implemented on Abaqus (ABAQUS Inc.) with the same compression procedure, boundary conditions, dimensions of the parts, and mechanical properties of the materials as in the actual experiments. Details of the

simulation are given in Supporting Information. Due to limitations in simulating the postbuckling behavior, the simulations stopped at around 2.25% of compression, which was, however, enough to obtain the initial stiffness and maximum buckling load. Notably, for both the experiments and simulations, the ABS caps at two ends of the struts were not included for simplicity. In addition, the effective lengths of the tubes were all 22 mm. For data analysis, the maximum buckling load was the maximum compression load. The initial stiffness of the struts against compression, which is the slope of the initial linear part of the curve, was calculated from the compression force divided by the displacement at 1% of compression. Please note that the unit of stiffness here is defined as  $\text{N mm}^{-1}$ . The MLB ratio was calculated from the maximum buckling load divided by the minimum compression force recorded after buckling.

*DS Tensegrity Compression Test and FEM Simulation:* The DS tensegrity modules were tested on Instron 5965 with a compression rate of  $20 \text{ mm min}^{-1}$  until 30% compression strain of the original heights (Figure 2B). The tensegrity was a 3D structure, meaning that it could be compressed in many directions. To quickly demonstrate its DS features, two types of compression tests were implemented: The first one was compressing from the top with a wooden plate pressing vertices 4–6 and vertices 1–3 facing the bottom. The initial height was 60 mm. Vertices 1–3 were fixed on three hinge joints; therefore, for each vertex, the three translations and the rotation in the plane perpendicular to hinge joint rotation plane were disallowed, while the rotation around the hinge joints and roll were free, as shown in Figure 2B(i). The purpose of the hinge joints was to avoid the noise in the force signal and reveal the clear stiffness characteristics of the tensegrity. During the top compression, the top and bottom triangles tended to twist with respect to each and thus, without the hinge joints, the vertices would slide on the plate, causing nontrivial noises. The second one was compressing from the side with vertices 3 and 6 contacting the wooden plate on top and the vertices 1, 2, 4, and 5 facing the bottom. The side compression was proceeded without the hinge joints as there was no sliding of the vertices and thus minor noise in the force signal. The initial height was also 60 mm. The tensegrity with CW twisting prism was chosen for testing and three samples were tested with three repetitions each. The FEM simulation of the tensegrity compression was also implemented on Abaqus (Figure 2C) with the same compression procedure, boundary conditions, dimensions of the parts, and mechanical properties of the materials. Details of the simulation are given in Supporting Information. Due to limitations in simulating the postbuckling behavior, the simulations stopped at around 9% and 25% of compression for top and side compression, respectively. For both tests, the maximum buckling load of the tensegrity module was recorded as the maximum compression force and the initial stiffness of the tensegrity module was calculated from the compression force divided by the displacement at 5% of compression.

*Compression and Crash Tests on the Tensegrity Robots:* Two types of compression tests (top and side compressions) were performed using Instron 5965 on the two DS tensegrity robots with a compression rate at  $20 \text{ mm min}^{-1}$  until 30% of compression. For the drone, the top compression was compressing from the top (Figure 3B) with an initial height of 90 mm (including the propellers), while, in the side compression test, the drone was placed in the orientation, as shown in Figure 3A.iv, with the force pressing along the short side (initial height = 130 mm) of the tensegrity frame. For the rover, the first compression was compressing from the top without the wheels (initial height = 60 mm) and, in the side compression test, the rover was placed in the orientation, as shown in Figure 4B, with an initial height of 160 mm. Unlike the tests on the struts and tensegrity modules, there was no fixation and the robots were placed in between two wooden plates. All experiments were repeated three times for each compression.

Please note that the choice of using CW and CCW tensegrity modules for the drone and rover bodies was mainly for symmetric body structures. With different tensegrity orientations, or using only one tensegrity assembly (either CW or CCW), robot bodies of other designs and shapes could be built. In this case, the top and side compressions may result in different stiffness characteristics due to the changes in the loading directions on the local tensegrity modules. However, despite the variations in the local stiffness, the global DS function remained.

The crash tests of the robots were performed at different heights from 40 cm with an increment of 20 cm until it broke. At each height, the test was repeated three times. All the crash tests were recorded by a high-speed camera (Chronos 1.4, Kron Technologies Inc.) at 240 fps for inspection and analysis on a motion analysis software (Tracker, Open Source Physics, ComPADRE.org).

## Supporting Information

Supporting Information is available from the Wiley Online Library or from the author.

## Acknowledgements

This work was partially funded by the Swiss National Science Foundation through the NCCR Robotics program and by the European Project H2020 Aerial Core.

## Conflict of Interest

The authors declare no conflict of interest.

## Data Availability Statement

The data that support the findings of this study are available from the corresponding author upon reasonable request.

## Keywords

dual stiffnesses, resilient robots, shell buckling, tensegrity robots

Received: January 25, 2022

Revised: March 20, 2022

Published online:

- [1] S. W. Squyres, R. E. Arvidson, E. T. Baumgartner, J. F. Bell, P. R. Christensen, S. Gorevan, K. E. Herkenhoff, G. Klingelhöfer, M. B. Madsen, R. V. Morris, R. Rieder, R. A. Romero, *J. Geophys. Res. Planets* **108**, **2003**, <https://doi.org/10.1029/2003JE002121>.
- [2] O. Khatib, X. Yeh, G. Brantner, B. Soe, B. Kim, S. Ganguly, H. Stuart, S. Wang, M. Cutkosky, A. Edsinger, P. Mullins, M. Barham, C. R. Voolstra, K. N. Salama, M. L'Hour, V. Creuze, *IEEE Rob. Autom. Mag.* **2016**, *23*, 20.
- [3] H. Li, A. V. Savkin, B. Vucetic, *Robotica* **2020**, *38*, 442.
- [4] J. Delmerico, S. Mintchev, A. Giusti, B. Gromov, K. Melo, T. Horvat, C. Cadena, M. Hutter, A. Ijspeert, D. Floreano, L. M. Gambardella, R. Siegwart, D. Scaramuzza, *J. Field Rob.* **2019**, *36*, 1171.
- [5] D. González, J. Pérez, V. Milanés, F. Nashashibi, *IEEE Trans. Intell. Transp. Syst.* **2015**, *17*, 1135.
- [6] M. T. Tolley, R. F. Shepherd, B. Mosadegh, K. C. Galloway, M. Wehner, M. Karpelson, R. J. Wood, G. M. Whitesides, *Soft Rob.* **2014**, *1*, 213.
- [7] N. W. Bartlett, M. T. Tolley, J. T. Overvelde, J. C. Weaver, B. Mosadegh, K. Bertoldi, G. M. Whitesides, R. J. Wood, *Science* **2015**, *349*, 161.
- [8] T. Li, Z. Zou, G. Mao, X. Yang, Y. Liang, C. Li, S. Qu, Z. Suo, W. Yang, *Soft Rob.* **2019**, *6*, 133.
- [9] C. Laschi, B. Mazzolai, M. Cianchetti, *Sci. Rob.* **2016**, *1*, eaah3690.
- [10] Y. Chen, H. Zhao, J. Mao, P. Chirarattananon, E. F. Helbling, N. S. P. Hyun, D. R. Clarke, R. J. Wood, *Nature* **2019**, *575*, 324.
- [11] Y. Sun, Y. S. Song, J. Paik, *2013 IEEE/RSJ Int. Conf. on Intelligent Robots and Systems (IROS)*, IEEE, Piscataway, NJ **2013**, pp. 4446–4453.
- [12] Y. Sun, X. Liang, H. K. Yap, J. Cao, M. H. Ang, R. C. H. Yeow, *IEEE Rob. Autom. Lett.* **2017**, *2*, 985.
- [13] U. Gupta, L. Qin, Y. Wang, H. Godaba, J. Zhu, *Smart Mater. Struct.* **2019**, *28*, 103002.
- [14] P. M. Kornatowski, A. Bhaskaran, G. M. Heitz, S. Mintchev, D. Floreano, *IEEE Rob. Autom. Lett.* **2018**, *3*, 3813.
- [15] P. M. Kornatowski, M. Feroskhan, W. J. Stewart, D. Floreano, *IEEE Rob. Autom. Lett.* **2020**, *5*, 4233.
- [16] S. Mintchev, D. Zappetti, J. Willemin, D. Floreano, *2018 IEEE/RSJ Int. Conf. on Robotics and Automation (ICRA)*, IEEE, Piscataway, NJ **2018**, pp. 7492–7497.
- [17] A. Briod, P. Kornatowski, J. C. Zufferey, D. Floreano, *J. Field Rob.* **2014**, *31*, 496.
- [18] P. Sareh, P. Chermprayong, M. Emmanuelli, H. Nadeem, M. Kovac, *Sci. Rob.* **2018**, *3*, eaah5228.
- [19] J. Zha, X. Wu, J. Kroeger, N. Perez, M. W. Mueller, *2020 IEEE/RSJ Int. Conf. on Intelligent Robots and Systems (IROS)*, IEEE, Piscataway, NJ **2020**, pp. 1407–1412.
- [20] S. Mintchev, S. de Rivaz, D. Floreano, *IEEE Rob. Autom. Lett.* **2017**, *2*, 1248.
- [21] S. Mintchev, J. Shintake, D. Floreano, *Sci. Rob.* **2018**, *3*, eaau0275.
- [22] M. Vespignani, J. M. Friesen, V. SunSpiral, J. Bruce, *2018 IEEE/RSJ Int. Conf. on Intelligent Robots and Systems (IROS)*, IEEE, Piscataway, NJ **2018**, pp. 2865–2871.
- [23] J. Rieffel, J. B. Mouret, *Soft Rob.* **2018**, *5*, 318.
- [24] H. Lee, Y. Jang, J. K. Choe, S. Lee, H. Song, J. P. Lee, N. Lone, J. Kim, *Sci. Rob.* **2020**, *5*, eaay9024.
- [25] D. Zappetti, S. H. Jeong, J. Shintake, D. Floreano, *Soft Rob.* **2020**, *7*, 362.
- [26] D. Zappetti, R. Arandes, E. Ajanic, D. Floreano, *Smart Mater. Struct.* **2020**, *29*, 075013.
- [27] S. Timoshenko, *Theory of Elastic Stability 2e*, Tata McGraw-Hill Education, New York, NY **1970**.